

Observations of the diurnal cycle of outgoing longwave radiation from the Geostationary Earth Radiation Budget instrument

Ruth E. Comer, Anthony Slingo, and Richard P. Allan

Environmental Systems Science Centre, University of Reading, UK

R. E. Comer, Environmental Systems Science Centre, Harry Pitt Building, 3 Earley Gate, Whiteknights, Reading. RG6 6AL. UK (rec@mail.nerc-essc.ac.uk)

The Geostationary Earth Radiation Budget instrument on Meteosat-8 provides unprecedented temporal sampling (~ 17 minutes) of the broadband emitted thermal and reflected solar radiances. We analyse the diurnal cycle of the outgoing longwave radiation (OLR) fluxes derived from the thermal radiances for July 2006. Principal component (PC) analysis separates the signals of the surface temperature response to solar heating and of the development of convective clouds. Most of the OLR variations are explained by the first two PCs: the first (surface heating) explains 82.3% of the total variance and the second (cloud development) explains 12.8% of the variance. Convection is initiated preferentially over mountainous regions and the cloud then advects downstream in the ambient flow. Diurnal variations are much weaker over the oceans, but a coherent signal over the Gulf of Guinea suggests that the cloudiness is modulated by the diurnally varying contrast between the Gulf and the adjacent land mass.

1. Introduction

The diurnal cycle of solar radiation represents one of the most significant modes of forcing of the climate system. The response to this forcing provides information on the physical processes acting at the surface and in the atmosphere, which must be represented accurately in weather and climate prediction models. The outgoing longwave radiation (OLR) measures the cooling of the planet to space and also provides a powerful diagnostic of the surface and atmospheric response to the diurnal solar forcing. Studies of the diurnal cycle of the OLR measured by satellites have therefore been made for many years, both to understand these physical processes and to evaluate models [see *Yang and Slingo*, 2001 for a review]. Many studies have analysed the OLR derived from narrow-band sensors on operational weather satellites in both sun-synchronous polar and geostationary orbits, often averaging several years of data to improve the statistics [e.g. *Gube*, 1982; *Yang and Slingo*, 2001; *Smith and Rutan*, 2003; *Nowicki and Merchant*, 2004]. *Smith and Rutan* [2003] used five years of data from the Earth Radiation Budget Satellite [ERBS; *Barkstrom et al.*, 1989]. This carried broad-band sensors, providing a more direct measure of the OLR, although the orbit took 72 days to precess through all local solar times.

Geostationary satellites clearly provide superior temporal sampling of OLR and data from multiple satellites can be combined to yield near-global coverage [*Yang and Slingo*, 2001; *Tian et al.*, 2004]. Even a limited data record from a single geostationary satellite can be used to study short-term variations over specific areas: for example, *Slingo et al.* [2004] analysed only 3 months of narrow-band radiances from Meteosat-7. This was made

possible by the improved time resolution of 30 minutes compared with the 3 hourly data used by *Yang and Slingo* [2001].

The new Geostationary Earth Radiation Budget (GERB) instrument on the Meteosat-8 satellite provides the first broad-band radiation budget measurements from geostationary orbit [*Harries et al.*, 2005]. The unprecedented temporal resolution of approximately 17 minutes enables a higher resolution investigation of the diurnal cycle of the OLR than has previously been possible. In this study, we analyse GERB data for July 2006. Following *Smith and Rutan* [2003], Principal Component (PC) analysis is used to investigate the diurnal cycle and the strengths and weaknesses of this approach are demonstrated. In general, it is seen that the first PC represents the land surface temperature response to the solar heating and the second PC represents the cloud response. The majority of the diurnal variations in the data can be described with just these first two PCs. The significance of topography for affecting the development of convective cloud is also evident. In some regions, however, there exists a more complex interaction between the radiative processes and moist dynamics, so this simple picture breaks down.

2. Data

This study uses one month of the Edition 1 release of the GERB OLR data for July 2006 in the ARG flux product (Averaged, Rectified, Geolocated). The ARG data have a time resolution of approximately 17 minutes and are provided on a grid with a resolution of 50km at nadir. The OLR radiances have an estimated absolute accuracy of 0.96%, while the angular modelling introduces an additional error estimated at 5 Wm^{-2} . Since the maximum OLR value in the data used here is about 390 Wm^{-2} , the error should be

less than 9 Wm^{-2} . In the present study, the data are interpolated onto a regular latitude-longitude grid with a resolution of 0.556 degrees in latitude and 0.833 degrees in longitude. This interpolation facilitates comparisons we have been making with the Met Office model [Allan *et al.*, 2005], as well as simplifying the current analysis method (see next section). Very similar results were obtained using preliminary GERB BARG (Binned, Averaged, Rectified, Geolocated) data for July 2004 [Comer *et al.*, 2006], but the more recent data are shown here because they have been released into the public domain. Further details of the GERB instrument and data processing are provided by Harries *et al.* [2005] and of the Meteosat-8 satellite by Schmetz *et al.* [2002].

3. Method

Empirical orthogonal functions (EOFs) and principal components (PCs) are calculated to describe respectively spatial and temporal variations in the data. The first PC describes the dominant signal in the data, having maximum possible temporal variation. Each subsequent PC describes the maximum variation of the data set after that of the preceding PCs has been removed. Each PC has a corresponding EOF, which shows where in the GERB view the variation associated with that PC is significant.

To create an average diurnal cycle the data are first linearly interpolated to every fifteen minutes, so that monthly means can be calculated for 96 regular intervals throughout the day. This diurnal cycle for July 2006 is then interpolated to local solar time (LST). The PCs and EOFs are computed following the method described by Smith and Rutan [2003]. For each pixel in the GERB field of view the overall mean is removed to provide a matrix of deviations, \mathbf{X} , with a row for each of the 96 times of day and a column for each pixel.

Each column of the matrix \mathbf{X} is multiplied by the square root of the area weight (the cosine of the latitude) of the pixel and a 96 by 96 covariance matrix is formed:

$$\mathbf{\Gamma} = \frac{\mathbf{X}\text{diag}(\mathbf{cos}\theta)\mathbf{X}^T}{\Sigma\mathbf{cos}\theta}, \quad (1)$$

where $\text{diag}(\mathbf{cos}\theta)$ is the diagonal matrix of area weights and $\Sigma\mathbf{cos}\theta$ is the sum of the area weights over the whole GERB view. The PCs ($\mathbf{c}_i, i = 1, \dots, 96$) are the eigenvectors of this covariance matrix, arranged according to descending eigenvalues (λ_i), and normalised so that $|\mathbf{c}_i|$ for each is equal to the square root of its eigenvalue λ_i . The relevant EOF (\mathbf{a}_i) for each PC is calculated from the PC and the data matrix:

$$\mathbf{a}_i = \frac{\mathbf{c}_i\mathbf{X}}{\lambda_i} \quad (2)$$

The study here differs from that of *Smith and Rutan* [2003] in that the land and ocean pixels are not separated out, but the domain is considered as a whole. The separation does not significantly affect the results and, as shown later, both land and ocean variations are well represented.

4. Results

Figure 1 shows the diurnal variations described by the first two PCs and their associated EOFs. The first PC describes 82.3% of the variation in the data and shows the response of the land surface temperature (and hence the OLR) to the solar heating. PC1 shows nocturnal cooling with a minimum shortly before dawn, followed by a rapid response to the solar heating up to a maximum at about 1300 Local Solar Time (LST). This

lag of the solar heating by approximately one hour is primarily due to the finite heat capacity of the surface, but is also influenced by atmospheric and surface feedbacks to the heating. After the maximum, the temperature declines as the solar input decreases to sunset, when the nocturnal cooling begins. This attribution of PC1 to surface heating was also found by *Smith and Rutan* [2003], although they noted that their first PC was “surprisingly symmetric” and required the addition of their second PC to produce the expected asymmetric behaviour. These effects are combined in our first PC, which perhaps illustrates the sensitivity of this analysis technique to the particular dataset employed; the result was unaffected by degrading the data to hourly resolution or restricting the analysis to land regions.

The first EOF (Figure 1b) shows that PC1 is largest over the deserts, which is where the diurnal surface temperature variations are greatest. Over the Saharan and Arabian deserts, the peak to trough amplitude in the OLR reaches close to 90 Wm^{-2} . The amplitude over the Kalahari is at most around 60 Wm^{-2} , because of the smaller insolation and surface heating in the Southern winter. Since surface solar heating over the desert is primarily responsible for the diurnal changes in the OLR, the mean diurnal cycle of the OLR here is nearly identical to that of PC1. This is illustrated for the Sahara in Figure 2a. Over the oceans, the amplitude of EOF1 is very small and generally not significant. There are coherent negative signals over the Gulf of Guinea and off the West coast of Africa, which are discussed later. Features in the Southern hemisphere on both EOF maps are due to episodic travelling synoptic systems that alias onto the diurnal PCs.

The diurnal cycle in clouds shows up clearly in the second principal component, PC2 (Figure 1c). This describes 12.8% of the diurnal variance, giving a total of over 95% of the variance explained by just the first two PCs. The main OLR signal in EOF2 is from convective cloud over land. The cloud is triggered by the surface heating (represented by the first PC) just after dawn and as it grows to a maximum extent at about 1700-1800 LST the OLR is forced to decrease as the cloud tops grow to higher, colder levels. After this time, the cloud gradually dissipates and the OLR increases again. This behaviour has been noted in previous studies, but the second EOF (Figure 1d) also shows that many of the strongest signals for the convective cloud are found over mountainous regions. This is illustrated further in Figure 3, which shows a comparison of the second EOF with a map of the topography in North Africa and the Arabian Peninsula. Peaks in EOF2 are seen to be associated with the Atlas mountains [1], the Ethiopian [2] and Cameroon highlands [3], the Hoggar [4], Tibesti [5] and Marra plateau [6], the Yemeni highlands [7] and several other smaller mountain ranges. This link between the topography and the OLR was also noted by *Yang and Slingo* [2001] in their Fourier analysis of narrow-band radiances. However, the present EOF analysis shows the influence much more clearly because, while a Fourier analysis reveals a shift in the phase of the diurnal cycle, the second EOF provides a direct measure of the significance in terms of the OLR.

Two bands are visible over North-East Brazil in Figure 1d which are also due to convective cloud. These were apparent in the analysis by *Garreaud and Wallace* [1997] of nine years of data from the International Satellite Cloud Climatology Project (ISCCP). The coastal band is a convective system, probably formed by the interaction of land-sea

breezes with the mean easterly flow [Kousky, 1980]. This system propagates inland and is reactivated the following evening to form the second distinctive band [Garreaud and Wallace, 1997; Cohen *et al.*, 1995]. Yang and Slingo [2001] pointed out that the phase of the diurnal harmonic becomes later in LST as mesoscale convective systems move away from their source (usually Westward in the tropics). This was reproduced in a Fourier analysis of the GERB data (not shown here), where the time of the maximum of the diurnal harmonic changes from around 0600 LST to 1100 LST over both North-East Brazil and the Ethiopian highlands.

EOF2 also shows negative values over the South Atlantic. This is due to low-level stratocumulus cloud, which is at its maximum extent (minimum OLR) just before dawn and is dissipated by solar heating, with a minimum extent (maximum OLR) in the late afternoon [Ciesielski *et al.* 2001]. The overall impact on the OLR is small (approximately 5 Wm^{-2}), because the cloud top is only slightly cooler than the ocean. Figure 2b shows that EOF2 is largely responsible for the mean diurnal cycle of the OLR in this region.

Using the two most significant principal components, it is possible to build up a reasonably accurate picture of the diurnal variations as a whole over most regions. For example, Figure 2c shows the mean variation over central Africa. The mean diurnal cycle is shown to have an earlier maximum than given by PC1. The combined contribution from the first two PCs provides a much closer fit to the overall mean. This illustrates the power of principal component analysis for representing physical variations. Over this region of Africa, PC1 explains the majority of the variation in the OLR, meaning that surface heating is dominant. However, the significant convective cloud signal from PC2 moves the overall

peak of the diurnal cycle to earlier in the day and produces a much faster decrease after noon as the cloud grows.

As mentioned earlier, the first EOF has some small areas of negative values around the coast of Africa. Since diurnal changes in ocean surface temperature are small [Weller and Anderson, 1996], the EOF1 signal here does not relate directly to the surface heating response. Instead, it is likely to relate to cloud development that is influenced by the adjacent heating of land regions. It can be seen from Figure 2d that the mean variation over the Gulf of Guinea does indeed have a significant daytime minimum and midnight maximum, but the shape of the curve is not similar to PC1. In fact the second and third PCs are both required to describe the variation. Plotting the mean OLR against local time over a series of days (not shown here) reveals that there is a regular daytime minimum, so this is not the result of a large synoptic system affecting the overall mean. The exact time of the minimum varies from day to day and tends to fall between 0400LST and 1600 LST. Daytime maxima in cloud amount both in the Gulf of Guinea and off the west coast of Africa have been noticed before [Duvel, 1989; Desbois *et al.*, 1988]. Desbois *et al.* suggested that this daytime maximum in cloud is forced by land-sea breeze effects.

5. Summary and Further Work

This first look at the diurnal cycle in GERB data highlights the effectiveness of high temporal resolution satellite data for exploring the diurnal cycle in the atmosphere and at the land surface. Principal component analysis proves a powerful tool for separating physical modes of variation such as surface and cloud responses. There is a clear orographic influence on the diurnal development of cloudiness over Africa. A coherent diurnal cycle

of convection over the northern coast of Brazil and the Gulf of Guinea is also found, suggesting a modulation by the diurnally varying contrast between land and ocean.

This quantitative assessment of OLR variations can readily be expanded using additional atmospheric observations, reanalyses and models. A specific application involves water vapour and its diurnal cycle in relation to that of clouds. Water vapour channel radiances from the SEVIRI imager [*Schmetz et al.*, 2002] are currently being analysed to study variations in upper tropospheric humidity. The methodology described in the present study can also be used to evaluate diurnal variations in numerical weather prediction and climate models, especially when the models have high spatial resolution.

Acknowledgments. The GERB data were obtained from the GERB Ground Segment Processing System (GGSPS) at Rutherford Appleton Laboratory. We thank fellow members of the GERB International Science Team for comments and suggestions throughout the study. R.E Comer was funded by a RETF/ESSC postgraduate grant.

References

- Allan, R. P., A. Slingo, S. Milton, and I. Culverwell (2005), Exploitation of Geostationary Earth Radiation Budget data using simulations from a numerical weather prediction model: Methodology and data validation, *J. Geophys. Res.*, *110*, doi: 10.1029/2004JD005698.
- Barkstrom, B., and Coauthors (1989), Earth Radiation Budget Experiment (ERBE) archival and april 1985 results, *Bull. Amer. Meteorol. Soc.*, *70*, 1254–1262.

- Ciesielski, P., W. Schubert, and R. Johnson (2001), Diurnal variability of the marine boundary layer during ASTEX, *J. Atmos. Sci.*, *58*, 2355–2376.
- Cohen, J., M. S. Dias, and C. Nobre (1995), Environmental conditions associated with Amazonian squall lines: A case study, *Mon. Weather Rev.*, *123*, 3163–3174.
- Comer, R. E., A. Slingo, and R. P. Allan (2006), The diurnal cycle observed by Meteosat-8 and simulated by a climate model, *EUMETSAT Meteorological Satellites Conference, Helsinki, Finland, Submitted*.
- Desbois, M., T. Kayiranga, B. Gnamien, S. Guessous, and L. Picon (1988), Characterization of some elements of the Sahelian climate and their interannual variations for July 1983, 1984 and 1985 from the analysis of METEOSAT ISCCP data, *J. Climate*, *1*, 867–904.
- Duvel, J. (1989), Convection over tropical Africa and the Atlantic ocean during northern summer. Part I: Interannual and diurnal variations, *Mon. Weather Rev.*, *117*, 2782–2799.
- Garreaud, R., and J. Wallace (1997), The diurnal march of convective cloudiness over the Americas, *Mon. Weather Rev.*, *125*, 3157–3171.
- Gube, M. (1982), Radiation budget parameters at the top of the earth's atmosphere derived from METEOSAT data, *J. Appl. Meteor.*, *21*, 1907–1921.
- Harries, J., and Coauthors (2005), The Geostationary Earth Radiation Budget (GERB) project, *Bull. Amer. Meteorol. Soc.*, *86*, 945–960.
- Kousky, V. (1980), Diurnal rainfall variation in northeast Brazil, *Mon. Weather Rev.*, *108*, 488–498.

- Nowicki, S., and C. Merchant (2004), Observations of diurnal and spatial variability of radiative forcing by equatorial deep convective clouds, *J. Geophys. Res.*, *109*, doi:10.1029/2003JD004176.
- Schmetz, J., P. Pili, S. Tjemkes, D. Just, J. Kerkman, S. Rota, and A. Ratier (2002), An introduction to Meteosat Second Generation (MSG), *Bull. Amer. Meteorol. Soc.*, *83*, 977–992.
- Slingo, A., K. Hodges, and G. Robinson (2004), Simulation of the diurnal cycle in a climate model and its evaluation using data from Meteosat 7, *Q. J. R. Meteorol. Soc.*, *130*, 1449–1467.
- Smith, G., and D. Rutan (2003), The diurnal cycle of outgoing longwave radiation from Earth Radiation Budget Experiment measurements, *J. Atmos. Sci.*, *60*, 1529–1542.
- Tian, B., B. Soden, and X. Wu (2004), Diurnal cycle of convection, clouds, and water vapor in the tropical upper troposphere: Satellites versus a general circulation model, *J. Geophys. Res.*, *109*, doi:10.1029/2003JD004117.
- Weller, R., and S. Anderson (1996), Surface meteorology and air-sea fluxes in the western equatorial Pacific warm pool during the TOGA coupled ocean-atmosphere response experiment, *J. Climate*, *9*, 1959–1990.
- Yang, G.-Y., and J. Slingo (2001), The diurnal cycle in the tropics, *Mon. Weather Rev.*, *129*, 784–801.

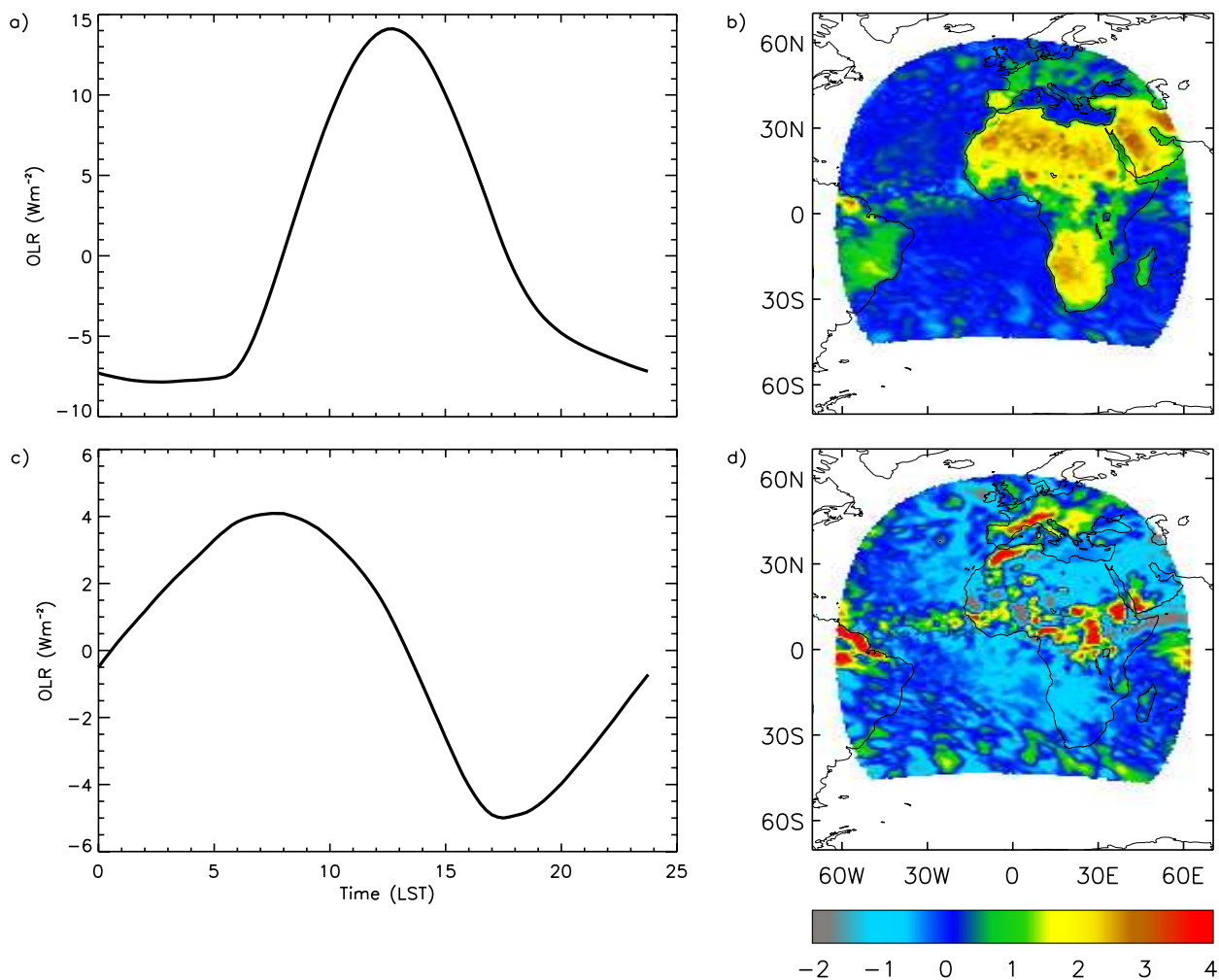


Figure 1. First two principal components of GERB data for July 2006 (a,c) together with their respective empirical orthogonal functions (b,d).

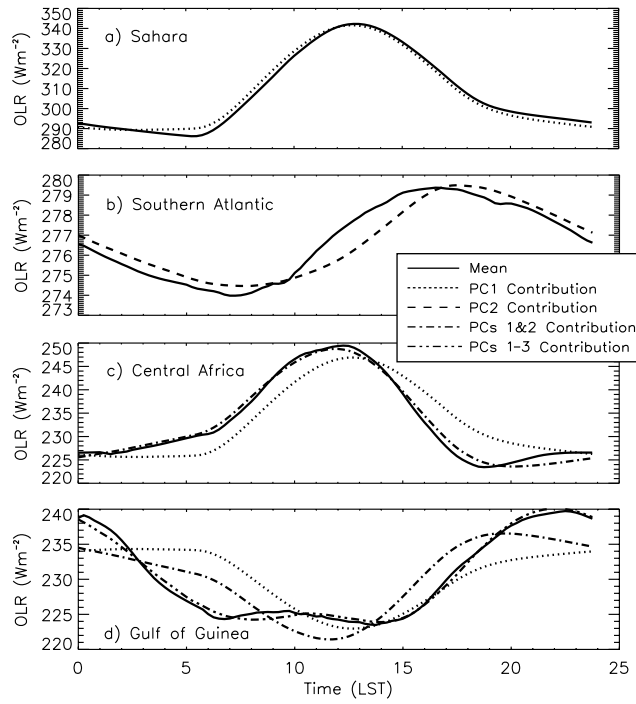


Figure 2. Comparisons of mean diurnal cycles (solid lines) with contributions from the principal components.

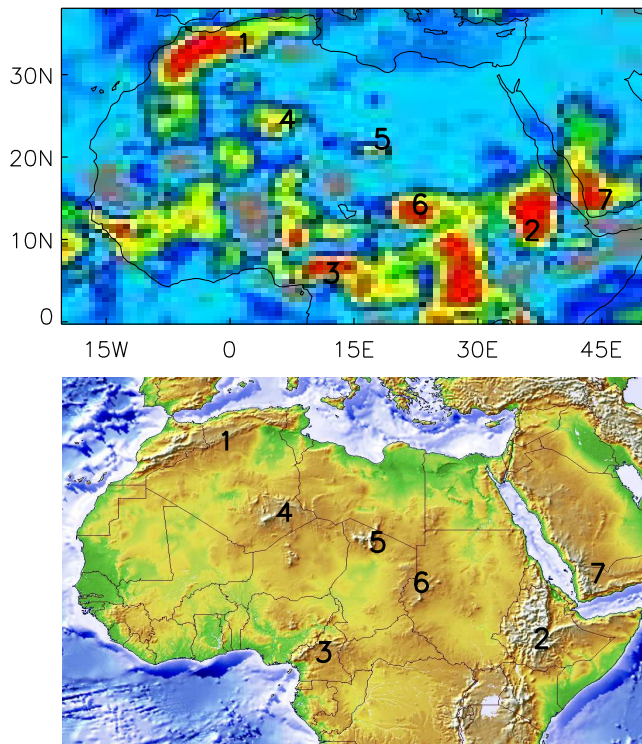


Figure 3. Comparison of the second empirical orthogonal function with topographical features in North Africa and the Arabian Peninsula (topographical map courtesy of UNEP/GRID-Arendal, <http://globalis.gvu.unu.edu/>).